

See discussions, stats, and author profiles for this publication at: <https://www.researchgate.net/publication/262194583>

The effect of fuel composition on the characteristics of a non-premixed synthetic natural gas-air flame

ARTICLE *in* FUEL PROCESSING TECHNOLOGY · OCTOBER 2014

Impact Factor: 3.35 · DOI: 10.1016/j.fuproc.2014.04.023

CITATIONS

3

READS

75

3 AUTHORS, INCLUDING:

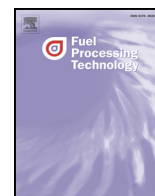


Jeongseog Oh

Korea Institute of Energy Research

17 PUBLICATIONS 109 CITATIONS

SEE PROFILE



The effect of fuel composition on the characteristics of a non-premixed synthetic natural gas-air flame

Jeongseog Oh ^{*}, Sanggeun Dong, Jebok Yang

Advanced Combustion Laboratory, Korea Institute of Energy Research, Daejeon, Republic of Korea

ARTICLE INFO

Article history:

Received 9 January 2014

Received in revised form 15 April 2014

Accepted 17 April 2014

Available online xxxx

Keywords:

Synthetic natural gas

Coaxial air

Non-premixed flame

Flame stabilization

Flame spectra

ABSTRACT

The variation of fuel composition in a non-premixed synthetic natural gas (SNG)-air flame was experimentally and numerically investigated in a lab-scale combustor with coaxial-type nozzles in order to determine the effect on flame stabilization and luminescence. Methane gas was blended with hydrogen and other hydrocarbon gases to modify the SNG, while compressed dry air was used as an oxidizer. The flow velocity at the nozzle exit was fixed at $u_F = 25$ m/s for fuel and $u_A = 0.17$ m/s for the oxidizer to measure flame behavior. Results showed that hydrogen addition to the fuel jet led to an increase in flame stabilization and a decrease in liftoff height. The maximum intensity of light emission was at a wavelength 308 nm. The adiabatic flame temperature increased with hydrogen addition to the fuel jet. The mole fraction of H_2O increased, while the mole fraction of CO_2 , CO , NO , and OH decreased with the addition of C_3H_8 and H_2 to the fuel jet.

© 2014 Elsevier B.V. All rights reserved.

1. Introduction

Concerns about increasing pollutant emissions and natural resource depletion have led to studies of synthetic gas (syngas) combustion as a clean coal combustion [1,2]. The most popular method to produce syngas is coal gasification or reforming low-rank coal. Coal gasification is known to be a carbon capture technology that is responsible for global warming and climate change. Integrated gasification combined cycle power plants are considered to be a substitute for traditional coal-fired power plants to improve thermal efficiency and achieve zero pollutant emission [2].

The use of syngas provides a practical use of low-rank coal, which was regarded as an economically useless resource for traditional coal-fired power plants in the past. In recent years, efforts have been made to use syngas as a form of synthetic natural gas (SNG), which is blended with natural gas. Hydrogen in syngas causes hydrogen brittleness in old city gas pipes, and SNG is a practical method because it can use syngas without retrofitting the existing pipeline network. Nevertheless, the characteristics of SNG flames are thought to differ from conventional natural gas because SNG is composed of hydrogen (H_2), methane (CH_4), and other hydrocarbon gases [3,4].

Walton et al. numerically and experimentally studied ignition delay times of oxy-syngas flames for application in a gas turbine combustor [5]. The volumetric ratio of hydrogen and carbon monoxide (H_2/CO)

gases varied from 0.25 to 4.0. They derived the experimental formula as a function of pressure (7.1–26.4 bar), temperature (855–1051 K), equivalence ratio (0.1–1.0), and oxygen mole fraction (15–20%). The ignition delay time increased with increasing temperature and decreased with the increase of pressure, equivalence ratio, and oxygen mole fraction.

Wu et al. numerically and experimentally investigated the laminar flame speed of various hydrocarbon-fueled mixtures (ethane, ethylene, acetylene, and CO) [6]. They reported that the flame speed increased with H_2 addition in reactive mixtures. For CO combustion, CO oxidation was accelerated by even small amounts of H_2 addition due to the strong catalytic influence of H_2 on the CO oxidation process.

Vu et al. numerically and experimentally studied cell formation and burning velocity of a laminar premixed syngas-air flame in a constant pressure combustion chamber with increasing surrounding pressure (P_∞) from $P_\infty = 1$ to 4 bar [7]. They found that cellular instability increased with increasing H_2 addition and preferential instability did not decrease with methane addition due to the decrease in the effective Lewis number.

Fu et al. experimentally studied the burning velocity of a laminar premixed syngas-air flame in a Bunsen burner [8]. They found that burning velocity and flame temperature increased while chemiluminescence intensity decreased with increasing hydrogen mole fraction in reactants ($X_{H_2} = 20$ –80%). From kinetic analysis, the hydrogen molecules carried out an important role in accelerating the chemical reaction.

In the current study, the variation of fuel composition in a non-premixed synthetic natural gas (SNG)-air flame was experimentally investigated in a lab-scale combustor with coaxial-type nozzles. Methane gas was blended with hydrogen and other hydrocarbon gases to

^{*} Corresponding author at: Advanced Combustion Laboratory, Korea Institute of Energy Research, Daejeon, Republic of Korea, 305–343. Tel.: +82 42 860 3479; fax: +82 42 860 3133.

E-mail address: jeongs5@kier.re.kr (J. Oh).

Nomenclature

A	pre-exponential factor (kgmol/m ³ /s)
a.u.	arbitrary unit
b	temperature exponent
CH*	chemiluminescence from methylidyne radicals (CH)
DO	discrete ordinates
DSLR	digital single lens reflex
d _A	outlet diameter at a coaxial air nozzle exit (mm)
d _F	outlet diameter at a fuel jet nozzle exit (mm)
ED	eddy-dissipation
EDC	eddy-dissipation concept
EVM	eddy viscous model
E _a	activation energy (J/kg/mol)
Fr _i	Froude number of species i ($= u_i^2 / (d_i \times g)$)
FL	focal length of a lens or spectrometer (mm)
f#	f-number of a camera or lens
g	acceleration of gravity (m/s ²)
H	liftoff height (mm)
ISO	international organization for standardization
I _λ	intensity of light emission (a.u.)
k _G	global reaction rate ($= AT_\infty^b \exp(-E_a/RT_\infty) [X_A]^m [X_B]^n$)
MFC	mass flow controller
MFM	mass flow meter
m, n	reaction order
OH*	chemiluminescence from hydroxide radicals (OH)
P _∞	atmospheric pressure (bar)
RANS	Reynolds averaged Navier–Stokes
Re _i	Reynolds number of species i ($= u_i \times d_i / \nu_i$)
RKE	realizable k-ε model
r	radial distance (mm)
SIMPLE	semi-implicit method for pressure linked equations
SNG	synthetic natural gas
T _{Ad}	adiabatic flame temperature (K)
T _A	coaxial air temperature (°C)
T _{co}	coflow air temperature (°C)
T _F	fuel jet temperature (°C)
T _∞	surrounding temperature (°C)
t _{exp}	exposure time of a camera (s)
t _{F,lip}	lip thickness of a fuel jet nozzle (mm)
t _{A,lip}	lip thickness of a coaxial air nozzle (mm)
u _A	coaxial air velocity at a nozzle exit (m/s)
u _{co}	coflow air velocity at a nozzle exit (m/s)
u _F	fuel jet velocity at a nozzle exit (m/s)
X _i	volumetric mole fraction of species i (%)
x	axial distance (mm)
ρ _i	density of species i (kg/m ³)
λ	wavelength of light emission (nm)
φ _G	global equivalence ratio
ν _i	kinematic viscosity of species i (m ² /s)
ω _i	reaction rate of specie i (kg/m ³ /s)

modify SNG, while compressed dry air was used as an oxidizer. Flame stabilization, flame luminescence, and temperature inside the lab-scale furnace were measured to study the effect of varying fuel compositions on flame characteristics.

2. Experimental methods

The experimental setup for the measurement of flame appearance, flame spectra, and time-averaged temperature comprised a lab-scale combustor, digital single lens reflex (DSLR) camera, spectrometer, and data acquisition (DAQ) system.

2.1. Lab-scale combustor

The internal dimensions of the lab-scale combustor were width 100 mm, depth 100 mm, and height 400 mm. Each wall was equipped with a quartz window to allow optical measurement. Coaxial-type nozzles were used for fuel in the center and for coaxial and coflow air. The diameter and lip thickness of the nozzle exit was $d_F = 2$ mm and $t_{F,lip} = 1$ mm, respectively, for the fuel jet and $d_A = 20$ mm and $t_{A,lip} = 12$ mm, respectively, for the coaxial air. Coflow air was injected around the coaxial air nozzle to fix global equivalence ratio (ϕ_G). Fig. 1 shows a schematic of the lab-scale combustor and a cross section of the fuel and coaxial air nozzles.

2.2. Flow rate regulation

The flow rate of the fuel jet and coaxial and coflow air was regulated with a mass flow meter (MFM) and mass flow controller (MFC) (5851E, Brooks Instrument Co., Hatfield, PA, USA). The MFM and MFC were controlled by Lab-VIEW modules (NI cDAQ 9172, NI 9263, and NI 9205; National Instruments Co., Austin, TX, USA) and the flow control system of the MFM, MFC, and Lab-VIEW modules was calibrated by a dry gas test meter (DA-16A-T; Sinagawa Co., Tokyo, Japan).

2.3. Visible flame measurement

A DSLR camera (D300s, Nikon Co., Tokyo, Japan) was used to take visible flame images and was mounted with a macro zoom lens (AF-S Nikkor, 24–70 mm, f/2.8; Nikon Co., Tokyo, Japan). The photographic conditions were f-number (f#) = 8, exposure time (t_{exp}) = 1/200 s, and light sensitivity ISO 1000.

2.4. Flame spectra measurement

A spectrometer (Acton SP2150i for grating body, spectra hub for signal controller, and PD471 for photo-diode; Princeton Instruments Inc., Trenton, NJ, USA) was used to analyze the spectral characteristics of a non-premixed SNG-air flame. The focal length of the spectrometer (FL) was 500 mm. Measuring wavelength (λ) was from 100 to 1000 nm. The flame spectra were measured five times at each condition at a resolution of 1 nm.

2.5. Experimental conditions

Flow velocity at the nozzle exit was varied as $u_F = 5$ –40 m/s for the fuel jet and $u_A = 0$ –0.43 m/s for the oxidizer to measure flame stabilization, while flow velocity at the nozzle exit was fixed at $u_F = 25$ m/s and $u_A = 0.17$ m/s to measure flame appearance, flame spectra, and time-averaged temperature. The fuel composition of the SNG is summarized in Table 1. Experiments were carried out at normal temperature $T_\infty = 300$ K and atmospheric pressure $P_\infty = 1$ bar. The Reynolds number of species i (Re_i) was defined as $Re_i = u_i \times d_i / \nu_i$, where ν_i is the kinematic viscosity of species i. The Froude number of species i (Fr_i) was defined as $Fr_i = u_i^2 / (d_i \times g)$, where g is the acceleration due to gravity. The test conditions are summarized in Tables 2 and 3.

3. Numerical methods

Numerical method were used to calculate the adiabatic flame temperature and mole fraction of products with a GasEq program [9] and the distribution of velocity, temperature, and species with a Fluent program [10] in a CH₄-air flame. Numerical results are helpful for compensating for the limitation of the experimental measurement if it is exactly predicted.

3.1. Governing equation

Governing equations were used to calculate the Eulerian gas-phase equation for the conservation of mass, momentum, energy, turbulent quantities, and species concentration. The conservation equation is expressed as a form of a differential equation to calculate implicit and explicit functions with a computer. The conservation equations for continuity, momentum (i.e. Navier–Stokes equation), and energy are as follows [10]:

$$\frac{\partial \rho}{\partial t} + \nabla \cdot (\rho \mathbf{u}) = 0 \quad (1)$$

$$\frac{\partial (\rho \mathbf{u})}{\partial t} + \nabla \cdot (\rho \mathbf{u} \mathbf{u}) = -\nabla p + \nabla \cdot \boldsymbol{\tau} + \rho \mathbf{g} \quad (2)$$

$$\frac{\partial (\rho C_p T)}{\partial t} + \nabla \cdot (\rho C_p T \mathbf{u}) = \nabla \cdot (k \nabla T) \quad (3)$$

where ρ is the density of species, t is the time, \mathbf{u} is the flow velocity, p is the pressure, $\boldsymbol{\tau}$ is the shear stress near the wall, \mathbf{g} is the acceleration due to gravity, T is the temperature, k is the thermal conductivity, and C_p is the specific heat.

3.2. Turbulence model

Turbulent viscous flow is a source of generating various-scale eddies. The kinetic energy of large-sized eddies is transferred to small-sized eddies due to vortex stretching. The kinetic energy of small-sized eddies is converted into thermal energy through an energy cascade by viscous dissipation. Reynolds-averaged Navier–Stokes (RANS) modeling is one method for predicting the energy cascade process in a turbulent viscous flow. An eddy viscous model (EVM) in the RANS modeling was used to solve the transport equation for mean flow quantities.

A realizable k - ε model (RKE) in the EVM modeling was used to simulate the flow field by isotropy assumption (i.e. Boussinesq approach) because streamlines, such as flows with swirling, high stretch (i.e. strain rate and curvature), or impingement (stagnation point) are not highly anisotropic. The turbulence transport equation is as follows [10]:

$$\frac{\partial (\rho k)}{\partial t} + \nabla \cdot (\rho k \mathbf{u}) = \nabla \cdot \left[\left(\mu + \frac{\mu_t}{Pr_k} \right) \frac{\partial k}{\partial x} \right] + G_k + G_b - \rho \varepsilon - Y_M \quad (4)$$

$$\frac{\partial (\rho \varepsilon)}{\partial t} + \nabla \cdot (\rho \varepsilon \mathbf{u}) = \frac{\partial}{\partial x} \left[\left(\mu + \frac{\mu_t}{Pr_\varepsilon} \right) \frac{\partial \varepsilon}{\partial x} \right] + \rho C_1 S_\varepsilon - \rho C_2 \frac{\varepsilon^2}{k + \sqrt{\nu \varepsilon}} + C_{1\varepsilon} \frac{\varepsilon}{k} C_{3\varepsilon} G_b \quad (5)$$

where k is the kinetic energy, ε is the eddy dissipation rate, μ_t is the turbulent eddy viscosity ($= \rho \times C_\mu \times k^2/\varepsilon$), C_μ is the variable that is determined in a mean velocity field ($= 0.09$ in an inertial sub layer near wall of $Sk/\varepsilon = 3.3$ and 0.05 in a shear layer of $Sk/\varepsilon = 6$), S is the strain rate ($= (2S_{ij}S_{ij})^{0.5}$), S_{ij} is the strain rate tensor, Pr_k and Pr_ε are the turbulent Prandtl number for k and ε ($= 1.0$ and 1.3 , respectively). G_k and G_b are the generation of turbulence due to mean velocity gradient and buoyancy, respectively, Y_M is the dilatation dissipation term ($= 2\rho \varepsilon Ma_\tau^2$) where Ma_τ is the turbulent Mach number. C_1 is the variables ($= \text{maximum of } [0.43, \eta/(\eta + 5)]$) where $\eta = Sk/\varepsilon$, C_2 and $C_{1\varepsilon}$ are the empirical constants ($= 1.92$ and 1.44 , respectively), and $C_{3\varepsilon}$ is the constant due to the effect of buoyancy on ε ($= \tanh|u_x/u_r|$) where u_x and u_r are the velocity component parallel and normal, respectively, to gravity direction.

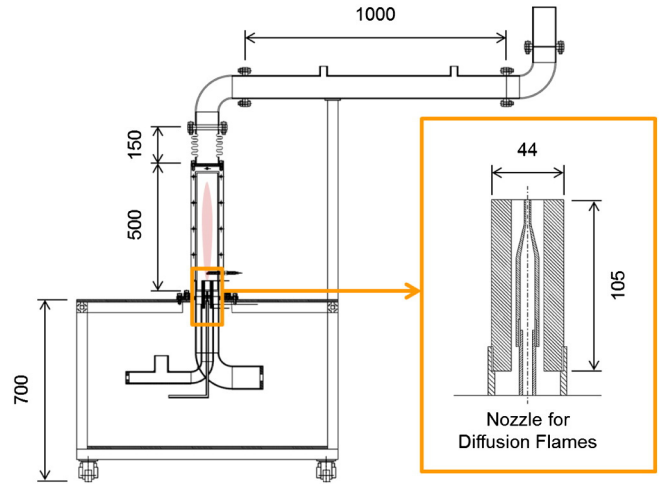


Fig. 1. Schematic of a lab-scale combustor and cross section of fuel and coaxial air nozzles (unit: mm).

3.3. Chemical reaction model

Combustion is defined as a fast chemical reaction generating heat, light, and pollutant emission. The total number of fluid-phase chemical species is conserved during transport processes from reactants to products. The sum of the mass fraction of species i becomes unity. The species transport equation is as follows [10]:

$$\frac{\partial (\rho Y_i)}{\partial t} + \nabla \cdot (\rho Y_i \mathbf{u}) = \nabla \cdot \mathbf{J}_i + R_i + S_i \quad (6)$$

where Y_i is the local mass fraction of species i , \mathbf{J}_i is the diffusion flux of species i , R_i is the net production rate of species i , and S_i is the addition rate from the dispersed phase. The equation for mass diffusion in the above equation is as follows [10]:

$$\mathbf{J}_i = -\rho D_{i,m} \nabla Y_i - D_{i,T} \frac{\nabla T}{T} \quad (7)$$

where $D_{i,m}$ is the mass diffusion coefficient for species i , $D_{i,T}$ is the thermal diffusion coefficient of species i , and T is the temperature.

The eddy-dissipation concept (EDC) model was used to simulate the turbulence-chemistry interaction. The EDC model is an extension of the eddy-dissipation (ED) model by considering detailed chemical mechanisms in a turbulent flow. The ED model uses a one or two-step heat-release mechanism without Arrhenius chemical kinetic calculations. Overall reaction rates are assumed to be controlled by turbulent mixing when reactants burn rapidly. The chemical reaction rate in the ED model is governed by a large-eddy-mixing time scale (k/ε). The net production rate of species i during a chemical reaction ($R_{i,r}$) is as follows [10]:

$$R_{i,r} = \text{minimum of} \left(A \nu'_{i,r} MW_i \rho \frac{\varepsilon}{k} \min \left(\frac{Y_R}{\nu'_{R,r} MW_R}, \frac{AB \nu'_{i,r} MW_i \rho \frac{\varepsilon}{k} \left(\frac{\sum_p Y_p}{\sum_j \nu'_{j,r} MW_j} \right)} \right) \right) \quad (8)$$

where Y_R and Y_P are the mass fraction of reactant and product species, respectively, $\nu'_{i,r}$ and $\nu''_{i,r}$ are the stoichiometric coefficient for reactant i and product i , respectively, in reaction r , A and B are the empirical constant ($= 4.0$ and 0.5 , respectively), and MW_i is the molecular weight of species i .

The EDC model assumes that a reaction occurs in fine-scale turbulent structures. The length fraction of the small turbulent structure is modeled as follows [10]:

$$\xi^* = C_\xi \left(\frac{\nu \mathcal{E}}{k^2} \right)^{0.25} \quad (9)$$

where $*$ denotes the fine-scale quantities, C_ξ is the volume fraction constant ($= 2.1377$), and ν is the kinetic viscosity. A reaction occurs in the volume fraction of a small turbulent structure (ξ^{*3}) and at a time-scale ($\tau^* = C_r(\nu/\varepsilon)^{0.5}$) where C_r is the time-scale constant ($= 0.4082$).

3.4. Radiation model

Radiation heat flux was considered with convective heat flux in the current calculation. Radiation heat transfer involves volumetric heat loss from an energy source to surroundings. A discrete ordinates (DO) radiation model was used to simulate the radiation heat transfer from a non-premixed SNG-air flame to walls in a lab-scale combustor by considering the absorption coefficient of flue gases. The DO model is known to be valid for various optical thicknesses of gases [10]. The radiation transport equation of the DO model is calculated with a finite volume method in control volumes, which is different to a ray-tracing model with a boundary element method. The radiation transport equation is as follows [10]:

$$\frac{d}{ds}I(\vec{r}, \vec{s}) + (a + \sigma_s)I(\vec{r}, \vec{s}) = an^2 \frac{\sigma T^4}{\pi} + \frac{\sigma_s}{4\pi} \int_{\Omega} I(\vec{r}, \vec{s}') \Phi(\vec{s} \cdot \vec{s}') d\Omega' \quad (10)$$

where s is the path length, I is the spectral radiation intensity, r is the position vector, s is the radiation direction vector, a is the spectral absorption coefficient, α_s is the scattering coefficient, n is the refractive index, σ is the Steffan-Boltzmann constant, T is the temperature, s is the scattering direction, Φ is the phase function, and Ω is the solid angle. Here, $(a + \alpha_s)s$ is the optical thickness.

A finite number of pixilation and a discrete solid angle in a control volume were 3×3 and 5×5 discrete ordinates for rotationally periodic boundaries. Each discrete ordinate has its own radiation direction in a solid angle. Emissivity from the walls was assumed as 0.8 when radiation was incident to the walls.

3.5. Boundary condition

Initial and boundary conditions were in agreement with experimental conditions, as shown in Table 3. The flow velocities at nozzle exits were $u_F = 25$ m/s, $u_A = 0.17$ m/s, and $u_{co} = 0.17$ m/s to fix $\phi_G = 0.5$ in all cases. The temperature on the steel wall and nozzle surface was fixed at 20 °C. Surrounding temperature and pressure were $T = 20$ °C and $P = 1$ bar, respectively. Turbulent intensity in a nozzle inlet and flow outlet was set to 1% and the turbulent viscosity ratio for the inlet and outlet was set to 5. These constants were configured again after the calculation of the cold-flow field.

Table 1
Fuel composition in SNG (unit: volumetric mole fraction, %).

Group	Mark	CH ₄	C ₂ H ₆	C ₃ H ₈	C ₄ H ₁₀	C ₅ H ₁₂	N ₂	H ₂
N gas	N0.0	92.46	5.00	1.46	0.65	0.02	0.40	0.0
	N1.0	91.05	4.93	1.96	0.65	0.02	0.40	1.0
	N3.0	88.26	4.78	2.94	0.63	0.02	0.38	3.0
C gas	C0.0	95.27	-	4.73	-	-	-	0.0
	C1.0	93.82	-	5.18	-	-	-	1.0
	C3.0	90.95	-	6.05	-	-	-	3.0
REF	CH4	100	-	-	-	-	-	-

Table 2
Experimental conditions for the flame stabilization map.

[illegible]

3.6. Numerical scheme

The algorithm of the semi-implicit method for pressure linked equations (SIMPLE) was used to increase resolution for the calculation of pressure-velocity coupling. Second-upwind methods were adapted to increase the calculation accuracy of governing equations and transport equations and a double-precision floating point was activated to increase solution accuracy.

3.7. Mesh generation

Two different-size structured meshes (i.e. a coarse grid (501,938 hexahedral cells) and dens grid (1,376,000 hexahedral cells)) were generated to simulate steady state cold and hot flow fields in the lab-scale combustor. Fig. 2 shows the isometric view of the coarse grid. The sensitivity and dependency analysis of grid size and grid number were tested by comparing velocity fields in cold flow conditions, as shown in Fig. 3(a) (i.e. coarse grid) and Fig. 3(b) (i.e. dense grid). Fig. 4 shows the velocity profile of numerical results at $x = 100$ and 200 mm and experimental results at $x = 200$ mm. The radial distribution of the velocity magnitude at $x = 200$ mm was well matched between numerical prediction and experimental measurement using an anemometer (9545; TSI inc., Shoreview, MN, USA). The coarse grid was employed for calculation economy in the current study.

4. Results and discussion

4.1. Flame stabilization

Flame stabilization is an important feature that is used to estimate combustor performance because the flame stabilization area is related to the operational range of the combustor.

Fig. 5 shows the flame stabilization map of a non-premixed SNG-air jet [11]. The mole fraction of fuel components was varied as shown in Table 1. The flame stabilization map for N gases, C gases, and CH₄ was divided into three regions: attached flame region, lifted flame region, and blow-off or blow-out region. The flame stabilization area (= attached flame region + lifted flame region) of N gases and C gases was broader than that of pure methane (CH₄). The stabilization area increased with the hydrogen mole fraction in the fuel jet. The deviation of the flame stabilization area was greater for the C gases than the N gases. This difference is thought to be due to the existence of high molecular

Table 3
Test conditions.

[illegible]

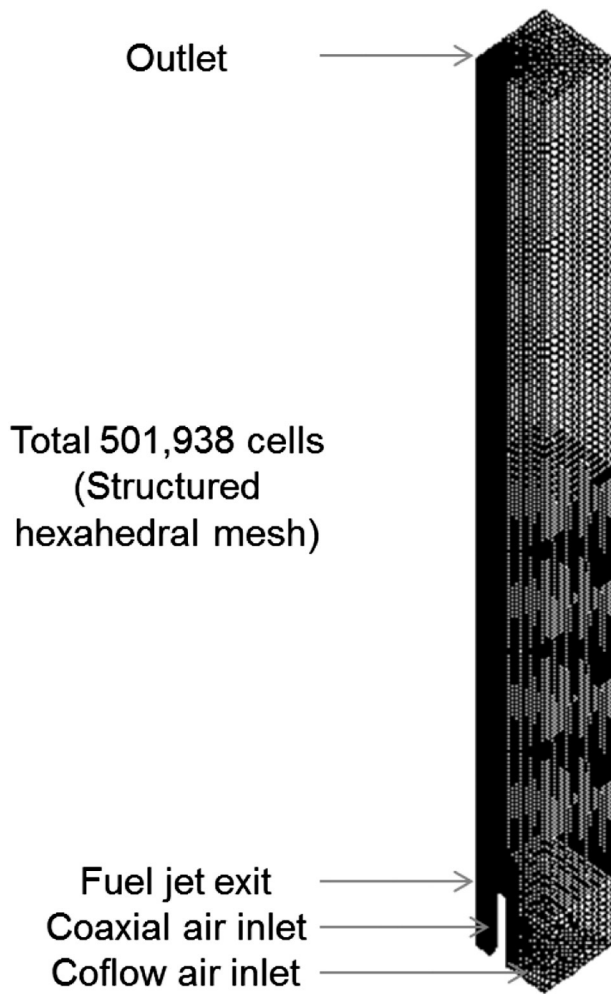


Fig. 2. Grid generation of a lab-scale SNG-air combustor.

hydrocarbon gases in the C gases even though the hydrogen mole fraction increased by the same proportion in the N gases and C gases.

Flame stabilization is related to the flame surface propagation velocity at the flame base [12,13]. If the burning velocity is equal to the local flow velocity at the flame base, a non-premixed SNG-air flame can be stabilized at a point called the flame stabilization point. The burning velocity at the stabilization point increases because the chemical reaction is activated by hydrogen. The lifted flame can be stabilized at a higher flow velocity by increasing the burning velocity. This effect leads to the broadening of the flame stabilization area.

4.2. Flame luminescence

Fig. 6 shows the visible flame appearance in relation to varying fuel compositions, in particular, the hydrogen mole fraction in the fuel jet [11]. The flame was blue around the flame base. Blue luminescence comes from the recombination of CO and O [14]. For the N gases, the flame base moved upstream as the hydrogen mole fraction increased in the fuel jet. For the C gases, however, the flame base moved downstream even though the hydrogen mole fraction increased in the fuel jet. This difference is due to the positive effect of hydrogen addition on burning velocity canceling out due to the increase of high molecule hydrocarbon gases in C gases.

Fig. 7 shows the trend of liftoff height behavior, which was extracted from the experimental results of the visible flame appearance as shown

in Fig. 6. The liftoff height (H) was defined as the distance from fuel jet nozzle exit to the flame base. The threshold value at the flame base was 30% of the maximum intensity in each visible image [15,16]. In general, the liftoff height of N gases and C gases was lower than that in a CH_4 -air flame. The liftoff height of N gases and C gases decreased with an increase in the hydrogen mole fraction in the fuel jet.

The location of the lifted flame base is known to move upstream as the burning velocity increases if the burning velocity is assumed to be in balance with the local flow velocity in the flame base [13]. It is thought that the addition of hydrogen into the fuel jet led to an increase in the burning velocity so that the liftoff height decreased due to an increase in the burning velocity under the same flow conditions [17]. The addition of high-weighted hydrocarbon fuel is thought to have negative effect on burning velocity because the liftoff height of the N gases was lower than that of the C gases at the same hydrogen mole fraction in the fuel jet.

Fig. 8 shows the flame spectra from a non-premixed SNG-air flame in Cases 1–6 (black solid line) and Case 7 (red solid line) [11]. The first peak of light emission was at $\lambda = 308 \text{ nm}$ and the first peak intensity was estimated to be $I_\lambda = 11,000\text{--}19,000 \text{ a.u.}$ in all cases. The second peak of light emission was at $\lambda = 283 \text{ nm}$ and the second peak intensity was estimated to be $I_\lambda = 5000$ in Cases 1 and 7. The second peak of light emission decreased significantly in Cases 2–6 compared to Case 7. This is thought to be due to a decrease in CH_4 and an increase in C_3H_8 and H_2 .

Wavelengths of 283 and 308 nm are known to be chemiluminescence from excited OH radicals (OH^*) [14,18]. Chemiluminescence intensity from excited CH radicals (CH^*) was relatively lower than that of the intensity of OH^* . OH^* was dominant light emission comparing with other wavelengths in the range of 100–800 nm in a non-

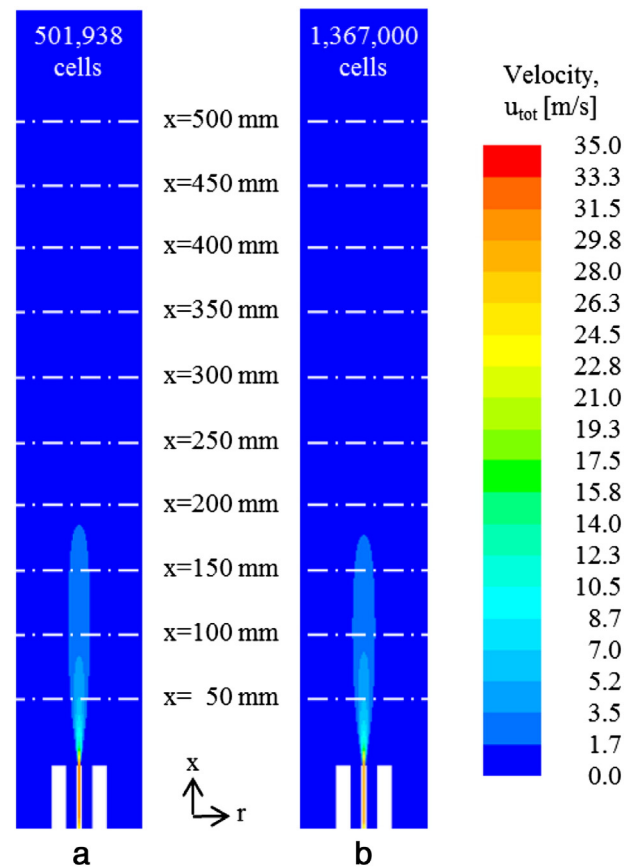


Fig. 3. Comparison of velocity distribution between (a) coarse grid (501,938 hexahedral cells) and (b) dense grid (1,376,000 hexahedral cells) under a cold flow conditions for testing grid dependency.

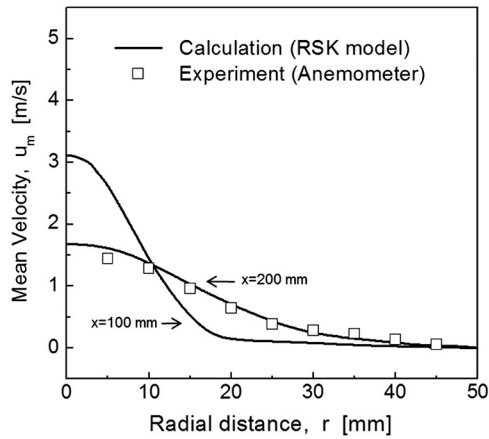


Fig. 4. Verification of the mean velocity profile from numerical prediction with a realizable $k-\epsilon$ model and experimental measurement with an anemometer.

premixed SNG-air flame. The distribution shape of the flame spectra was similar for both, while the peak intensity of minor species was different depending on the flow conditions, as shown in Fig. 8.

OH^* and CH^* were used as an indicator of the heat release rate in a reaction zone [19–22]. The chemical process of OH radicals is known to be a result of the recombination between O and H atoms [23]. The intensity of OH^* is known to be affected by the mass flow rate of a fuel, surrounding pressure, and the global equivalence ratio [24].

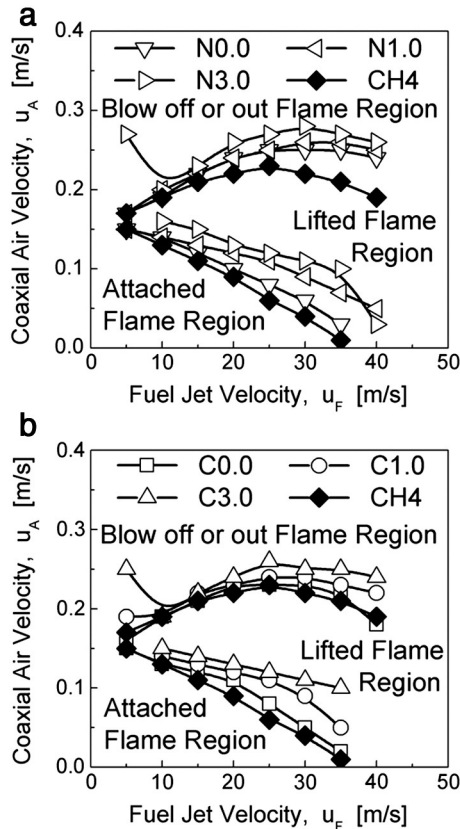


Fig. 5. Flame stability map composing of attached flame region, liftoff flame region, and blow-off or blow-out region: (a) N gases and CH_4 and (b) C gases and CH_4 [27].

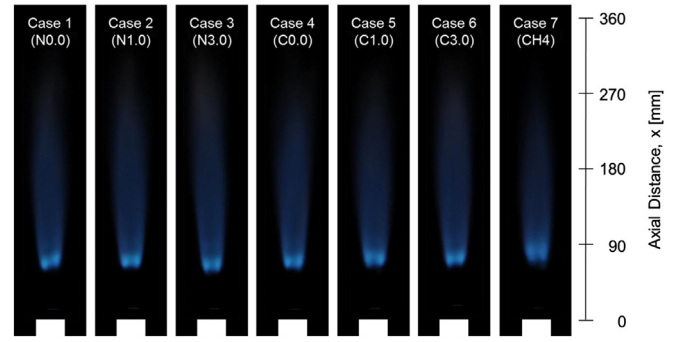


Fig. 6. Visible flame appearance of coaxial air and SNG diffusion flames with varied fuel compositions under the conditions of $u_F = 25$ m/s and $u_A = 0.17$ m/s [27].

4.3. Reaction process

Numerical simulation was performed to investigate the internal flow field (i.e. hot flow condition) with a Fluent program [10]. A refined two-step reaction mechanism was used for the chemical kinetic modeling of methane oxidation, as summarized in Table 4. This two-step mechanism is known to be more useful than that in one-step reaction mechanism for predicting adiabatic flame temperature because it includes the dissociation process during methane oxidation [24–26].

Fig. 9 shows the distribution of total velocity magnitude, total temperature, and kinetic rate of reaction steps (R1–3) in a CH_4 -air flame (i.e. Case 7). Here, total means the sum of static and dynamic values. The velocity magnitude of the hot flow in Fig. 9(a) increased compared to the cold flow in Fig. 3(b) at the same location. This is thought to be due to an increase in total temperature, as shown in Fig. 9(b). The temperature increase involves heat expansion and leads to a density decrease under constant pressure conditions. Temperature distribution is thought to be affected by specific heat because specific heat is dependent on the chemical species during the conversion from reactants to products.

The reaction of CH_4 and O_2 (i.e. R1) occurred upstream in Fig. 9(c) before the reaction of CH_4 and O_2 (i.e. R2) occurred downstream in Fig. 9(d). The dissociation process of CO_2 to CO and O (i.e. R3) is plotted in Fig. 9(e). The oxidation of hydrocarbon fuel affiliated with alkanes ($\text{C}_n\text{H}_{2n+2}$) are known to follow the process: (1) decomposition to alkene (C_nH_{2n}) and H_2 by O and H atoms, (2) unsaturated alkenes oxidation to CO and H_2 , and (3) CO and H_2 oxidation to CO_2 and H_2O [27]. Most heat release occurred during CO oxidation (i.e. $\text{CO} + \text{OH} \rightarrow \text{CO}_2 + \text{H}$).

Fig. 10 shows the comparison of mean velocity magnitude between hot flow (red solid line) and cold flow (black solid line), which was

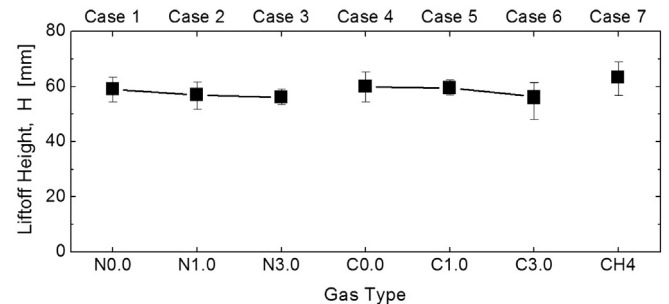


Fig. 7. Trend of liftoff height in a non-premixed SNG-air flame (extracted from the measurement of visible flame appearance in Fig. 6).

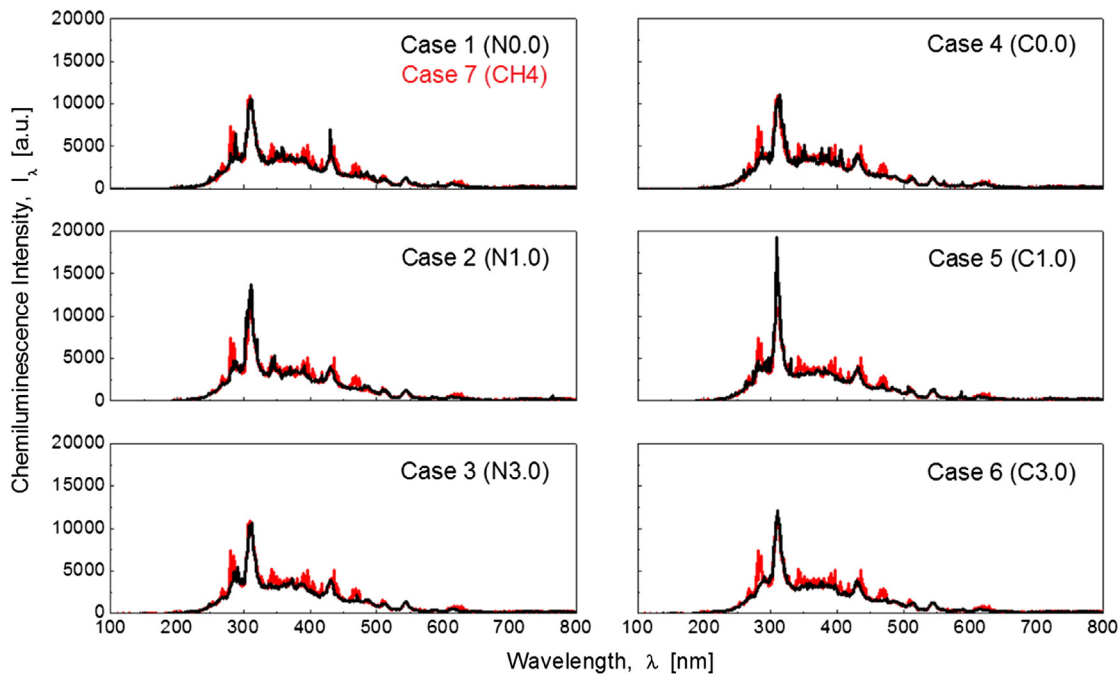


Fig. 8. Light emission spectrum of various composed SNG diffusion flames under the conditions of $u_f = 25$ m/s and $u_A = 0.17$ m/s; Cases 1–6 (black) and 7 (red) [27].

extracted along the centerline in Fig. 8(a). The velocity decreased exponentially after injecting from nozzle in both cases. The velocity gradient and magnitude of the hot flow was steeper and lower than that of the cold flow below the lifted flame base (Fig. 9). Moreover, the velocity magnitude increased slightly at $x = 70$ – 190 mm from the flame base to the center and declined modestly after $x = 190$ mm. This is thought to be due to the effect of buoyancy and flow redirection near the lifted flame base [13,28].

4.4. Adiabatic flame temperature

Fig. 11 shows the adiabatic flame temperature of SNG–air combustion in relation to the global equivalence ratio. In general, the adiabatic temperature increased with the global equivalence ratio of $\phi_G = 0.4$ – 1.0 , while the temperature decreased with an increase in the global equivalence ratio to $\phi_G = 1.0$ – 2.0 . Maximum temperature was predicted as $T_{Ad} = 2230.6$ – 2233.6 K at $\phi_G = 1.0$.

The adiabatic flame temperature increased with the addition of hydrogen into the fuel (Fig. 11). The temperature of N gases was higher than that of the C gases. The adiabatic temperature of C0.0 was lowest, while the adiabatic temperature of N0.0 was highest. The temperature difference in the N gases, C gases, and CH₄ was less than 5 K. The positive effect of the hydrogen addition on the increase of flame temperature was thought to be reduced due to the increase in C₃H₈, as shown in Table 1, instead of methane.

This tendency of the adiabatic flame temperature is thought to be related to the size of the reaction zone because the reaction rate is

dependent on flame temperature. Previous researchers studied the effect of hydrogen addition on the flame length of a non-premixed oxy-methane flame [29]. It was reported that the addition of hydrogen into a fuel jet accelerated the chemical reaction and it led to a local increase in flame temperature. Moreover, hydrogen blending to methane flames has a positive effect to reduce ignition temperature due to enhancing reaction activity [17]. Combustion efficiency increased and CO emission decreased as increasing hydrogen addition in a fuel jet [30]. Meanwhile, hydrogen-enriched methane flame has a negative effect on CO formation when flame temperature is lower than 800 °C [17].

4.5. Flame structure

Fig. 12 shows the distribution of the volumetric mole fraction (X_i) of major species (i.e. O₂, CH₄, CO, CO₂, and H₂O) in a CH₄–air flame (Case 7). Hydrocarbon fuel reacted with surrounding air, as shown in Figs. 12(a) and (b), and reactants were converted into products (Figs. 12(c), (d), and (e)). This means that methane combustion involves primary CO production (i.e. methane pyrolysis) and then secondary CO oxidation into CO₂. Hydrogen-containing species are known to play an important role in CO oxidation ($\text{CO} + \text{OH} \rightarrow \text{CO}_2 + \text{H}$) [27]. The effect of third-body collisions and backward reactions on CH₄–air combustion was not considered in the current study. The area of the H₂O mole fraction in Fig. 10(e) was wider than that of CO₂ in Fig. 12(d), while the area of the CO₂ mole fraction was similar to that of the temperature distribution in Fig. 9(b).

Table 4

Refined two-step reaction mechanism for CH₄ oxidation (here, $k_G = A T^b \exp(-E_a/RT_\infty) [X_A]^m [X_B]^n$).

Number	Chemical reaction	Pre-exponential factor, A [kgmol/m ³ /s]	Temperature exponent, b	Activation energy, E _a [J/kgmol]	Reaction order, $[X_A]^m [X_B]^n$
R1	$\text{CH}_4 + 1.5\text{O}_2 \rightarrow \text{CO} + 2\text{H}_2\text{O}$	5.012×10^{11}	0	2.0×10^8	$[\text{CH}_4]^{0.7} [\text{O}_2]^{0.8}$
R2	$\text{CO} + 0.5\text{O}_2 \rightarrow \text{CO}_2$	2.239×10^{12}	0	1.7×10^8	$[\text{CO}] [\text{O}_2]^{0.25} [\text{H}_2\text{O}]^{0.5}$
R3	$\text{CO}_2 \rightarrow \text{CO} + 0.5\text{O}_2$	5.0×10^8	0	1.7×10^8	$[\text{CO}_2]$

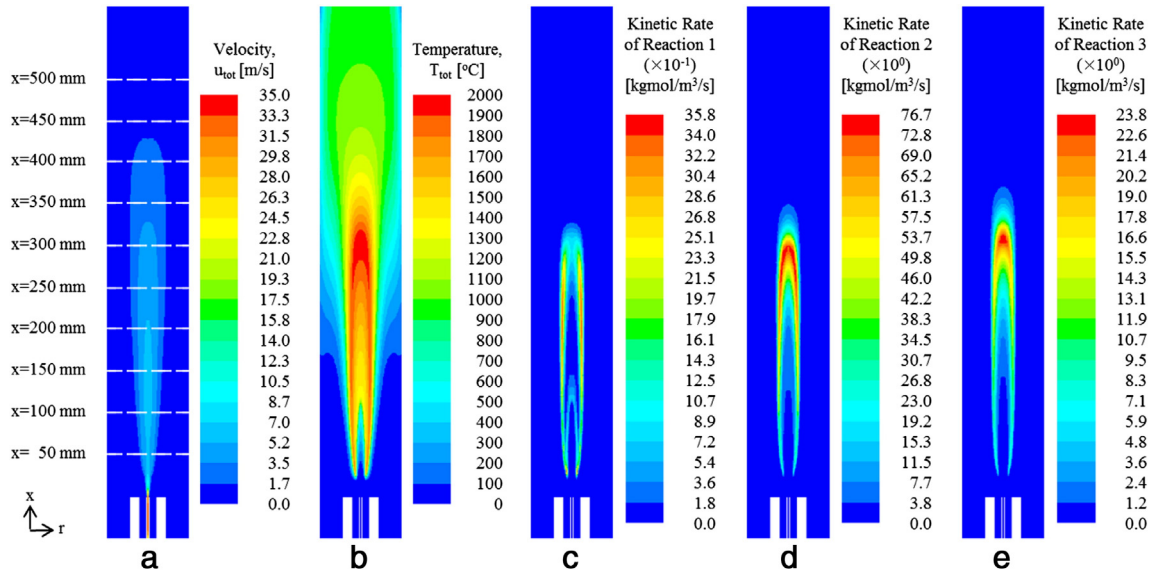


Fig. 9. Hot flow field in a CH₄-air flame (Case 7): the distribution of (a) total velocity magnitude, (b) total temperature, and kinetic rate of reaction steps for (c) R1, (d) R2, and (e) R3.

Fig. 13 shows the mole fraction (Y_i) of products as a result of SNG-air combustion in Cases 3 (black solid line) and 7 (red solid line); this was calculated with a Gaseq program [9]. In general, the mole fraction of H₂O increased, while the mole fraction of CO₂, CO, NO, and OH decreased with the addition of C₃H₈ and H₂ in the fuel jet.

The major species (H₂O, CO₂, CO, O₂, and H₂) variation trend was plotted as the increasing global equivalence ratio in Fig. 13 (upper panel). The mole fraction of H₂O and CO₂ was maximized near a stoichiometric condition due to complete combustion. Meanwhile, the mole fraction of CO and H₂ was kept nearly constant at $\phi_G = 0.4$ –1.0 and then it increased with the global equivalence ratio at $\phi_G = 1.0$ –2.0. This is thought to be the result of a water-gas shift reaction ($\text{CO} + \text{H}_2\text{O} \rightarrow \text{CO}_2 + \text{H}_2$) in a fuel-rich region [27].

The trend of minor species (OH, H, O, and NO) variation was plotted as the increasing global equivalence ratio in Fig. 13 (lower panel). The minor species increased in the fuel-lean region and decreased in the fuel-rich region with increased global equivalence ratio. The condition of the maximum mole fraction was $\phi_G = 0.8$ for NO molecules, $\phi_G = 1.0$ for OH molecules, $\phi_G = 0.9$ for O atoms, and $\phi_G = 1.2$ for H atoms.

The trend of the OH mole fraction was similar to the chemiluminescence intensity from excited OH radicals (OH*) in a previous work [31]. The O and OH atoms are known to be related to the chemical reaction kinetics of NO formation [27].

5. Conclusions

In the current study, the variation of fuel composition in a non-premixed SNG-air flame was experimentally investigated in a lab-scale combustor with coaxial-type nozzles. Methane was blended with hydrogen and other hydrocarbon gases to modify the SNG, while compressed dry air was used as an oxidizer. Flame stabilization and flame luminescence were measured to study the variation effect on flame characteristics. From the above measurements, the conclusions are summarized as follows:

- (1) Increasing the hydrogen mole fraction in the fuel jet broaden the flame stabilization area. The variation in the flame stabilization area was more significant in C gases than in N gases.

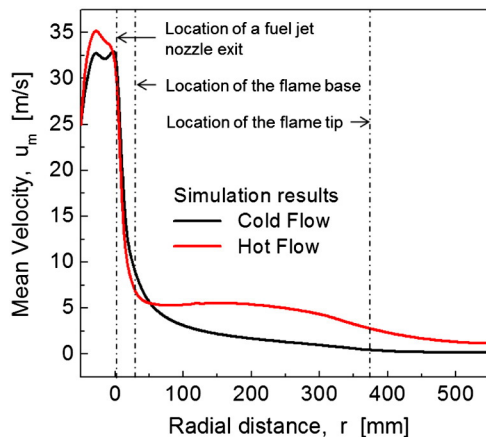


Fig. 10. Comparison of velocity profiles along the centerline between a cold flow in Fig. 3(a) and a hot flow in Fig. 8(a).

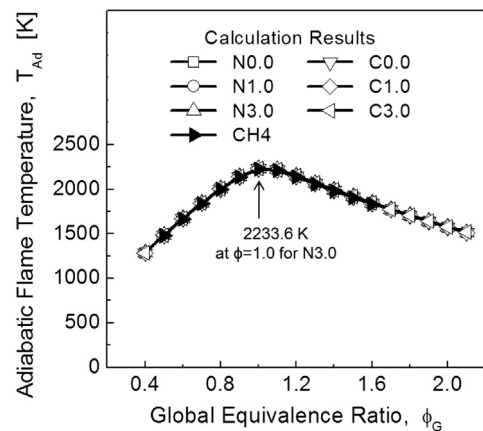


Fig. 11. Adiabatic flame temperature of SNG-air combustion in relation to global equivalence ratio.

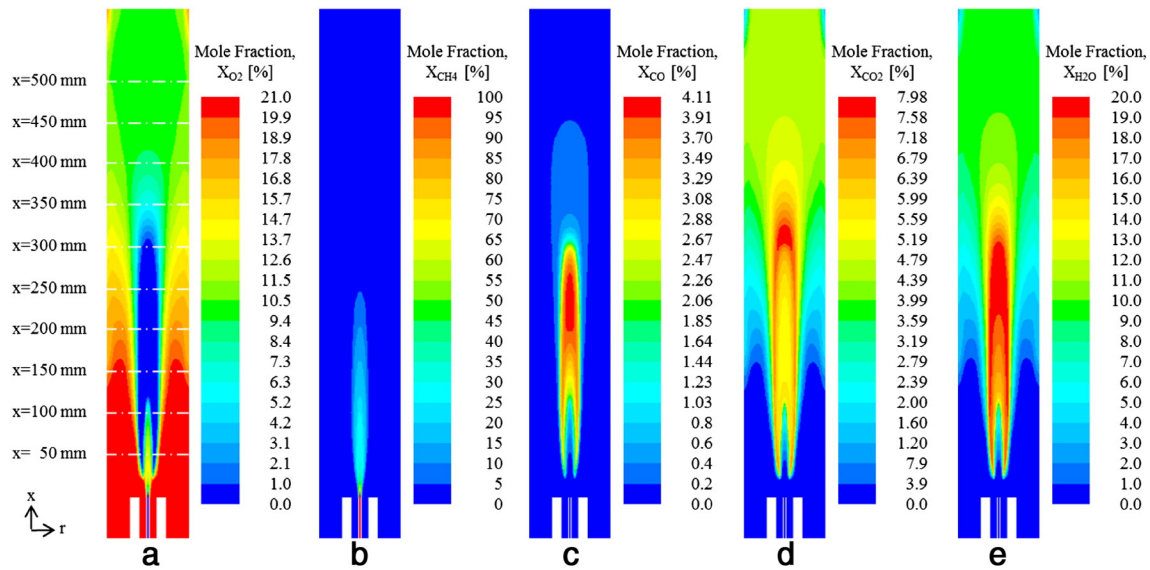


Fig. 12. Volumetric mole fraction (X_i) of major species in a CH_4 -air flame (Case 7): the distribution of (a) O_2 , (b) CH_4 , (c) CO , (d) CO_2 , and (e) H_2O .

- (2) The liftoff height for the N gases decreased with an increase in the hydrogen mole fraction in the fuel jet. The liftoff height for the C gases did not show a significant difference due to an increase in the high molecule hydrocarbon gases in the fuel jet.
- (3) The maximum intensity of light emission was at $\lambda = 308$ nm, which was due to OH radicals. The second peak intensity was at the wavelength (λ) of $\lambda = 430$ nm which was responsible for CH radicals.
- (4) The flame structure and species distribution of a lifted CH_4 -air flame (Case 7) was numerically simulated with Gaseq and Fluent programs. The adiabatic flame temperature increased with hydrogen addition to the fuel jet. The mole fraction of H_2O increased, while the mole fraction of CO_2 , CO , NO , and OH decreased with the addition of C_3H_8 and H_2 to the fuel jet.

References

- [1] A. Holmen, O. Olsvik, O.A. Rokstad, Pyrolysis of natural gas: chemistry and process concepts, *Fuel Processing Technology* 42 (1995) 249–267.
- [2] F. Delattin, G.D. Lorenzo, S. Rizzo, S. Bram, J.D. Ruyck, Combustion of syngas in a pressurized microturbine-like combustor: Experimental results, *Applied Energy* 87 (2010) 1441–1452.
- [3] J.G. Wünnig, A. Milani, Handbook of burner technology for industrial furnaces-fundamentals burner applications, Vulkan-Verlag GmbH, Huysenallee, Essen, Germany, 2009.
- [4] K.K.J.R. Dinesh, X. Jiang, W. Malalasekera, A. Odedra, Large eddy simulation of fuel variability and flame dynamics of hydrogen-enriched nonpremixed flames, *Fuel Processing Technology* 107 (2013) 2–13.
- [5] S.M. Walton, X. He, B.T. Zigler, M.S. Wooldridge, An experimental investigation of the ignition properties of hydrogen and carbon monoxide mixtures for syngas turbine applications, *Proceedings of the Combustion Institute* 31 (2007) 3147–3154.
- [6] F. Wu, A.P. Kelley, C. Tang, D. Zhu, C.K. Law, Measurement and correlation of laminar flame speeds of CO and C_2 hydrocarbons with hydrogen addition at atmospheric and elevated pressures, *International Journal of Hydrogen Energy* 36 (2011) 13171–13180.
- [7] T.M. Vu, J. Park, J.S. Kim, O.B. Kwon, J.H. Yun, S.I. Keel, Experimental study on cellular instabilities in hydrocarbon-hydrogen-carbon monoxide-air premixed flames, *International Journal of Hydrogen Energy* 36 (2011) 6914–6924.
- [8] J. Fu, C. Tang, W. Jin, L.D. Thi, Z. Huang, Y. Zhang, Study on laminar flame speed and flame structure of syngas with varied compositions using OH-PLIF and spectrograph, *International Journal of Hydrogen Energy* 38 (2013) 1636–1643.
- [9] , Website address <http://www.gaseq.co.uk/gseqdnd.htm>.
- [10] ANSYS Inc., ANSYS FLUENT 12.0 theory guide, Canonsburg, USA, 2009.
- [11] J. Oh, S. Dong, J. Yang, Characteristics of non-premixed synthetic natural gas-air flame with variation in fuel compositions, *Transaction of KSME B37* (9) (2013) 829–836.
- [12] S.H. Chung, Stabilization, propagation and instability of tribrachial triple flames, *Proceedings of the Combustion Institute* 31 (2007) 877–892.
- [13] J. Oh, Y. Yoon, Flame stabilization in a lifted non-premixed turbulent hydrogen jet with coaxial air, *International Journal of Hydrogen Energy* 35 (2010) 10569–10579.
- [14] A.G. Gaydon, The spectroscopy of flames, 2nd edition Chapman and Hall, London, UK, 1974.
- [15] J. Oh, D. Noh, Lifted flame behavior of a non-premixed oxy-methane jet in a lab-scale slot burner, *Fuel* 103 (2013) 862–868.
- [16] J. Oh, D. Noh, The effect of CO_2 addition on the flame behavior of a non-premixed oxy-methane jet in a lab-scale furnace, *Fuel* 117 (2014) 79–86.
- [17] K. Zhao, D. Cui, T. Xu, Q. Zhou, S. Hui, H. Hu, Effects of hydrogen addition on methane combustion, *Fuel Processing Technology* 89 (2008) 1142–1147.
- [18] S. Cheski, A. Goldman, Laser diagnostics of trace species in low-pressure flat flame, *Progress of Energy and Combustion Science* 35 (2009) 365–382.
- [19] J. Oh, P. Heo, Y. Yoon, Acoustic excitation effect on NOx reduction and flame stability in a lifted non-premixed turbulent hydrogen jet with coaxial air, *International Journal of Hydrogen Energy* 34 (2009) 7852–7861.
- [20] J. Oh, J. Hwang, Y. Yoon, EINOx scaling in a non-premixed turbulent hydrogen jet with swirled coaxial air, *International Journal of Hydrogen Energy* 35 (2010) 8715–8722.
- [21] A.G. Gaydon, H.G. Wolfhard, *Flames – Their structure, radiation and temperature*, 3rd edition Chapman and Hall, London, UK, 1970.

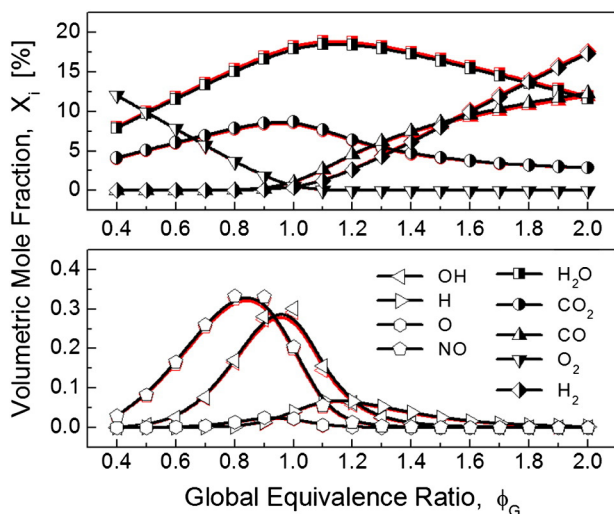


Fig. 13. Volumetric mole fraction of products of SNG-air combustion in relation to global equivalence ratio in Cases 3 (black) and 7 (red).

- [22] B. Higgins, M.Q. McQuay, F. Lacas, J.C. Rolon, N. Darabiha, S. Candel, Systematic measurements of OH chemiluminescence for fuel-lean, high-pressure, premixed, laminar flames, *Fuel* 80 (2001) 67–74.
- [23] C.Y. Liu, G. Chen, N. Sipöcz, M. Assadi, X.B. Bai, Characteristics of oxy-fuel combustion in gas turbines, *Applied Energy* 89 (2012) 387–394.
- [24] D.J. Hautman, F.L. Dryer, K.P. Schug, I. Glassman, A multiple-step overall kinetic mechanism for the oxidation of hydrocarbons, *Combustion Science and Technology* 25 (1981) 219–235.
- [25] C.K. Westbrook, F.L. Dryer, Simplified reaction mechanisms for the oxidation of hydrocarbon fuels in flames, *Combustion Science and Technology* 27 (1981) 31–43.
- [26] J. Zhang, W. Pratiño, L. Zhang, Z. Zhang, Computational fluid dynamics modeling on the air-firing and oxy-fuel combustion of dried Victorian brown coal, *Energy & Fuels* 27 (2013) 4258–4269.
- [27] S. Turns, *An introduction to combustion: concepts and applications*, 3rd ed. McGraw-Hill, New York, 2012.
- [28] J. Oh, Y. Yoon, Liftoff height behavior in a non-premixed turbulent hydrogen jet with coaxial air, *Fuel* 91 (2012) 134–140.
- [29] J. Oh, D. Noh, C. Ko, The effect of hydrogen addition on the flame behavior of a non-premixed oxy-methane jet in a lab-scale furnace, *Energy* 62 (2013) 362–369.
- [30] M. Ilbas, I. Yılmaz, Experimental analysis of the effects of hydrogen addition on methane combustion, *International Journal of Energy Research* 36 (2012) 643–647.
- [31] M. Orain, Y. Hardalupas, Effect of fuel type on equivalence ratio measuring using chemiluminescence in premixed flames, *Comptes Rendus Mecanique* 338 (2010) 241–254.